climate

MDPI

Article

Propagation Speed Climatology of Pacific Equatorial Kelvin Waves in Different Background Conditions

Crizzia Mielle De Castro * and Paul E. Roundy

Department of Atmospheric and Environmental Sciences, University at Albany, Albany, NY 12222, USA; proundy@albany.edu

* Correspondence: cdecastro@albany.edu

Abstract

Atmospheric equatorial Kelvin waves—convective disturbances that manipulate tropical wind and rainfall patterns—can propagate eastward at speeds ranging from nearly stationary to 30 m/s, with variability determined by moist processes and advection by the background wind. Current studies on Kelvin waves lack a comprehensive climatology that explains how their structure and propagation speeds change in different background states. Thus, this work builds a variable regression model that uses ERA5 reanalysis data to reconstruct Kelvin waves during different background wind shear conditions and phases of the Madden–Julian Oscillation (MJO) and the El Niño–Southern Oscillation (ENSO) over the Pacific. Overall, Kelvin waves tend to speed up during background conditions that generate upper-tropospheric westerlies and slow down during upper-tropospheric easterlies. East Pacific Kelvin waves are faster than West Pacific Kelvin waves because of climatological westerly shear in the former and easterly shear in the latter. However, strong westerly shear over the East Pacific allows extratropical Rossby waves to impede on the Kelvin wave, while strong easterly shear over the West Pacific distorts classical Kelvin wave structure. The results provide references for weather prediction models to accurately resolve the interaction between Kelvin waves and background circulation.

Keywords: convectively coupled Kelvin waves; Madden–Julian Oscillation; El Niño–Southern Oscillation; propagation speeds; Pacific Ocean; equatorial waves

1. Introduction

Atmospheric convectively coupled Kelvin waves—organized disturbances characterized by in-phase geopotential and zonal winds propagating eastward along the equator—manipulate wind and rainfall patterns across the tropics [1]. They can span horizontal structures of 3000–6000 km in scale and propagate eastward at speeds ranging from nearly stationary to 30 m/s [2–4]. The substantial variability of observed Kelvin wave propagation speeds emerges from the combined action of moist processes and acceleration by the background wind [5–7]. Kelvin waves also interact differently with the background environment at varying heights, leading to a diverse range of phase speeds propagating eastward together, with convection tying circulations across the troposphere complicating wave steering. Other studies have shown that a Kelvin wave's lower-tropospheric component responds strongly to the convective moisture source that powers and organizes the wave [8,9]. On the other hand, the upper-tropospheric component acts as a forced response to convection from the lower troposphere, forming a unified vertical structure. However,

Check for updates

Academic Editor: Haikun Zhao

Received: 13 February 2026
Revised: 20 April 2026
Accepted: 21 April 2026
Published: 24 April 2026

Copyright: © 2026 by the authors. Licensee MDPI, Basel, Switzerland. This article is an open access article distributed under the terms and conditions of the Creative Commons Attribution (CC BY) license.

not all components of the Kelvin wave across the troposphere continue propagating eastward. The Kelvin wave may leave behind or distort some of its associated circulation and pressure disturbances as it experiences different background conditions [10–13]. Furthermore, Kelvin wave propagation speeds can vary as they encounter regions with stronger or weaker coupling between their dynamic and convective components, such as passing through the Amazon [14] or through Africa [11].

Stronger upper-tropospheric winds tend to allow only the fastest Kelvin waves to retain their classical structure, while weaker winds in the lower troposphere may cause weaker acceleration and less variability in Kelvin wave propagation speeds. Instead, variability in lower-tropospheric Kelvin wave propagation speeds may arise from convective heating and moist processes changing the static stability felt by the wave [7,15]. As saturated air parcels condense moisture and increase buoyancy, the reduced static stability may decrease the Kelvin wave's vertical restoring force, leading to slower propagation speeds. Kelvin wave phase speeds can also be affected by major intraseasonal to interannual convective disturbances in the tropics, including the Madden–Julian Oscillation (MJO) and El Niño–Southern Oscillation (ENSO). Both the MJO and ENSO can modify the background wind shear [16,17] and background moisture states through changes in deep convection [18] and sea surface temperatures [19,20].

Previous works have shown a strong relationship between the background flow and Kelvin waves in the stratosphere [6], through an idealized global model [21], and with respect to the vorticity budget [8]. Furthermore, the structures of Kelvin waves can deviate from classical theory [22] due to differences between their propagation (phase) speeds and the background flow [6] and intrusions of extratropical Rossby waves caused by strong background westerlies [10,23]. Kelvin wave intensity and propagation speed variability have also been attributed to changes in the phase of the MJO [24] and ENSO [23,25]. However, current works lack a comprehensive propagation speed climatology of Kelvin waves influenced by intraseasonal changes in the background flow and moisture states. Kelvin waves introduce potential predictability on subseasonal timescales, but even the best numerical weather prediction models struggle to properly represent their statistics [26,27], making them propagate too fast, leading to weaker associated circulation and precipitation [3]. A comprehensive Kelvin wave phase-speed climatology can assess their relationship with the background environment, provide benchmarks for numerical weather prediction accuracy, and inform rainfall forecasts of deep convection.

Thus, this work builds a variable regression model that uses information from reanalysis data to predict the structure and phase speeds of Kelvin waves during different convective phases of the MJO and ENSO, and background vertical wind shear. Here, we assess the relationship between the structure and phase speeds of atmospheric Kelvin waves and background conditions at different geographical locations and heights. This work answers the following questions: (1) How do Kelvin wave structures and phase speeds vary depending on geographical location, phase of the MJO and ENSO, and background wind shear? And (2) How do Kelvin wave structures and phase speeds compare between their upper- and lower-tropospheric components?

2. Data and Methods

To represent convection, daily average outgoing longwave radiation (OLR) data were provided by the NOAA Climate Data Record with 1.0 × 1.0-degree spatial resolution [28]. Daily average geopotential, specific humidity, and zonal and meridional winds were also obtained from the ERA5 reanalysis with 0.25 × 0.25-degree spatial resolution and pressure levels at 850 hPa and 200 hPa [29]. All data included in the analysis span 1979 to 2020. To get anomalies, a linear regression model was applied to remove the long-term mean

and the first three harmonics of the seasonal cycle. Background winds were considered as zonal winds fluctuating at periods of 30 days or longer, calculated by applying a 30-day period low-pass Fourier filter to the total (not anomalous) zonal winds that included all wavenumbers. Background vertical wind shear was calculated as the background winds at 200 hPa minus the background winds at 850 hPa. The daily real-time multivariate MJO (RMM) indices and phases were obtained from the IRI Climate Data Library following Ref. [30]. We used the RMM indices to track the geographical location of the MJO's enhanced and suppressed convection and primary zonal circulation. Lastly, we used the monthly Niño 3.4 indices from the IRI Climate Data Library to track ENSO phases. The Niño 3.4 indices indicate the average sea surface temperature (SST) anomalies within 5° N–5° S and 170° W–120° W using the SST archive by Ref. [31]. Linear interpolation was applied to convert from a monthly to daily temporal resolution, where the given Nino 3.4 indices were set as the 15th of each month, and a linear transition from one month to the next was assumed.

To isolate the region of the power spectrum dominated by Kelvin wave signals from regions dominated by other equatorial waves, we used a modified version of Fourier filtering applied to OLR anomalies following Ref. [32]. This work refrains from separating symmetric and antisymmetric signals about the equator to include commonly observed asymmetric Kelvin wave signals. We also used a broad rectangular mask to extract Kelvin wave signals with frequencies between 0.05 and 0.33 (or periods 3 to 20 days) and wavenumbers 2 to 9. This approach can include eastward advected equatorial Rossby waves or Kelvin waves deviating from their classical structure, but these can be distinguished by their spatial structures. To address the issue of reconstructed disturbances containing other signals besides Kelvin waves, we applied a correlation test between the geopotential and zonal wind fields around the base longitude. We applied simple linear correlations to calculate the average correlation coefficients between the geopotential and zonal winds at 15° E to 15° W and 5° N to 5° S centered at the base longitudes. Positive correlations above the 10th percentile of positive coefficients during the zeroth time lag indicate reconstructed disturbances consistent with Kelvin waves. Strong positive correlations indicate mostly in-phase geopotential and zonal winds, while negative correlations indicate out-of-phase geopotential and zonal winds. Through correlation analysis, we can assess the consistency of signals reconstructed by variable regression with classical Kelvin waves.

A modified variable coefficient regression model following Refs. [6,33] was used to reconstruct wave signals in different background conditions. Unlike simple linear regression models, variable regression includes information on background conditions, allowing us to predict the dynamical structure of wave signals at specific background conditions and base longitudes. Ref. [33] allowed the regression coefficients to be functions of the seasonal cycle, but this work allows the regression coefficients to vary with the background wind shear or RMM and Niño 3.4 indices. The variable regression model applies two regressions, one in the context of the other. The first regression assesses the relationship between the Fourier-filtered OLR and the dynamical fields (winds and geopotential) through their covariance and variance. The second regression builds the covariance and variance as functions of background variables. Calculating regression coefficients this way determines how the relationship between the Fourier-filtered OLR and dynamical fields changes with the background variables. Figure 1 shows a conceptual framework diagram summarizing how the variable regression model assesses the response of the filtered wave disturbance to changes in the background environment.

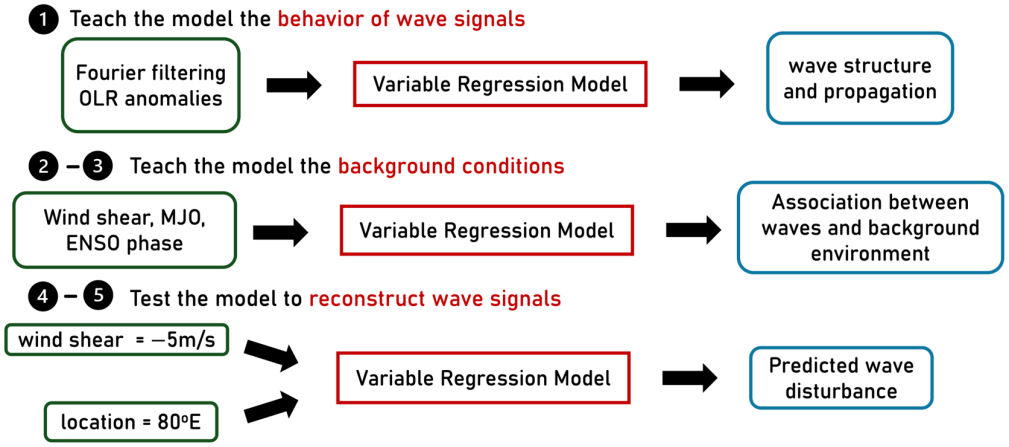


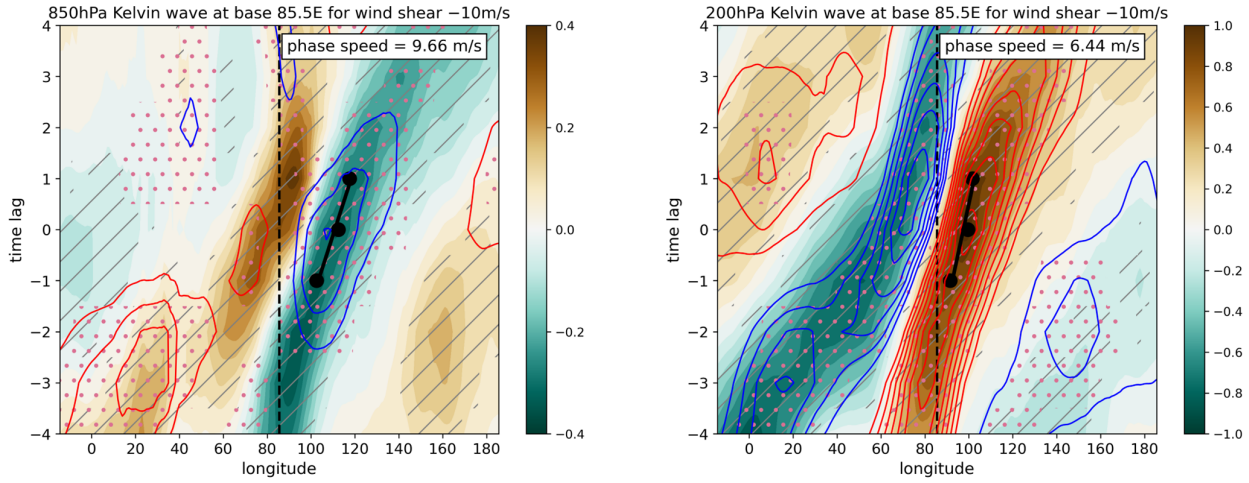
Figure 1. Conceptual framework diagram of the variable regression model used to reconstruct wave disturbances in different background conditions and geographical locations. Step 4 shows a sample user input for assessing the wave's response to easterly wind shear over the East Indian Ocean.

1. In the first regression, the predictor matrix is set as x = Fourier-filtered OLR, and the predictand is set as y = unfiltered dynamical and OLR fields. We used OLR, zonal and meridional wind, and geopotential anomalies as predictand y. The variance at the base longitude is calculated as $Y_{var} = x_{base} \cdot x_{base}$, while covariance is calculated as $Y_{covar} = x_{base} \cdot y$
2. To build the second regression of the model, a variable predictor matrix X was formulated following $X = [1, X_o, X_o^2, X_o^3]$. The variable predictor X_o corresponds to different background wind shear, RMM indices, or Nino 3.4 indices.
3. The regression coefficients of the covariance are calculated as $m_{covar} = (X^T X)^{-1}(X^T X_{covar})$, while the regression coefficients of the variance are calculated as $m_{var} = (X^T X)^{-1}(X^T X_{var})$. Using these regression coefficients, the model can now reconstruct wave signals in different background conditions.
4. A new predictor matrix $X_{new} = [1, x_o, x_o^2, x_o^3]$ corresponds to the background condition of interest. For example, we can choose $x_o = 5$ m/s for westerly background wind shear or $x_o = -1.5$ for strong La Niña conditions. The new covariance and variance are predicted as $X_{covar} = X_{new} \cdot m_{covar}$ and $X_{var} = X_{new} \cdot m_{var}$, respectively.
5. The final coefficients are calculated as $m = \frac{X_{covar}}{X_{var}}$ and scaled by the negative of one standard deviation $-\sqrt{X_{var}}$. When plotted in maps, the coefficients show the associated wave dynamics during the chosen background condition.

The variable regression model can reconstruct associated dynamical fields (winds, geopotential, and OLR) of wave signals at a user-specified base longitude and background condition along four dimensions (x, y, z, and t): longitude, latitude, height, and time. However, the model enforces an important caveat—it cannot accurately predict wave disturbances in background conditions outside the range of previously observed background conditions at each base longitude. Thus, we consider the West and East Pacific basins separately, because these two regions have vastly different background flow distributions. We also applied simple linear regressions to get the total 200 hPa zonal winds, as well as the 850 hPa specific humidity and zonal winds associated with different background wind shear and RMM and Niño 3.4 indices.

Hovmöller (longitude vs. time) diagrams were used to track the eastward propagation of regressed disturbances and calculate their phase speeds (Figure 2 shows samples). They were obtained through time-lagged variable regressions of zonal wind fields centered at each prescribed base longitude. As illustrated in Figure 2, the disturbance's phase speed equates to the slope of the best-fit line of three points (day before, day of, and day after) as

the wave passes through the base longitude. We used only three points when calculating the phase speeds to ensure that we could get the localized response of the disturbance while having adequate points to form a best-fit line. The disturbance would respond to different background environments if we extend the calculations farther from the base longitude. A more localized phase speed calculation about the base longitude also ensures that we get the strongest associated winds with the strongest statistical stability. To separate the phase speeds between their lower- and upper-tropospheric components, we follow the eastward propagation of the maximum easterlies at 850 hPa and the maximum westerlies at 200 hPa. To build a phase speed climatology, Hovmöller diagrams of regressed zonal winds were repeated at different background wind shears, RMM indices, and Niño 3.4 indices for different base longitudes over the West Pacific (60–130° E) and East Pacific (200–270° E). This grid-based approach for detecting and tracking Fourier-filtered waves has been successfully applied in other studies [3,15] and is comparable with other studies that use object tracking methods [9,34]. Furthermore, we assessed the robustness of our methods to detect, track, and reconstruct wave disturbances through statistical tests.



(**a**) 850 hPa Kelvin wave (**b**) 200 hPa Kelvin wave

Figure 2. Hovmöller diagrams of zonal winds (shading) and geopotential (3 m^2s^{-2} contours) associated with an (**a**) 850 hPa and (**b**) 200 hPa reconstructed wave passing through base longitude 85.5° E (dashed vertical line) during background vertical wind shear −10 m/s. Red and blue contours indicate positive and negative anomalies, respectively. Hatches and pink dots indicate statistically significant zonal wind and geopotential, respectively, at 95% confidence. Phase speeds were calculated following the best-fit line at time lag −1, 0, 1 (black dots).

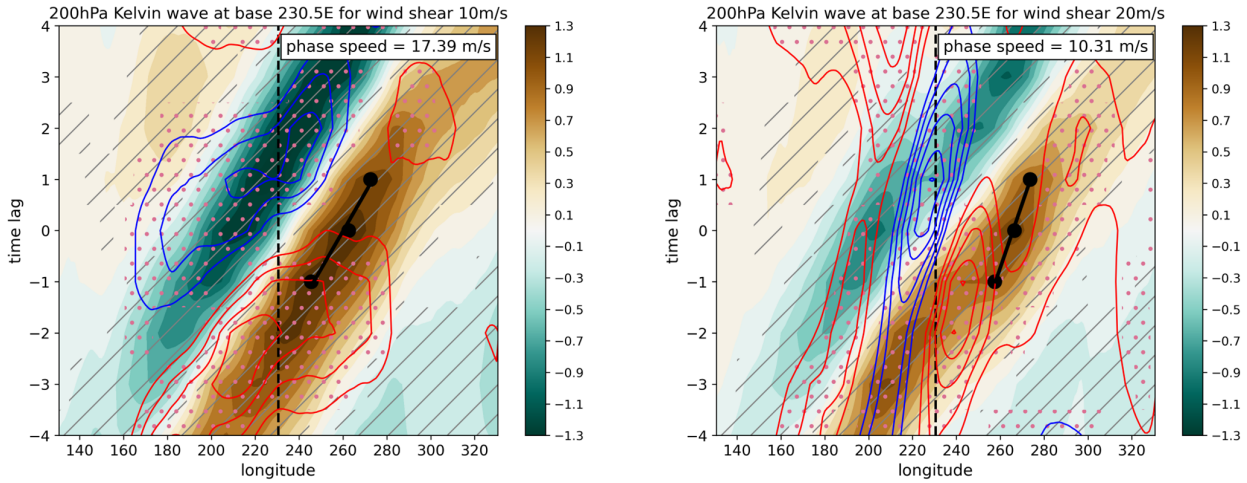
Monte Carlo experiments following Ref. [35] test if the calculated phase speeds are statistically different from zero with the null hypothesis of no difference. The approach creates artificial Fourier transforms composed of random real and imaginary parts with the same power spectrum to replace the actual Fourier-filtered OLR, which assesses the possibility that random chance could explain the original signals. The power spectrum is obtained by applying a Fourier transform to the Fourier-filtered OLR and then multiplying by its complex conjugate. The power spectrum is composed of the sum of the squares of its real and imaginary parts, i.e., $Power = (Re)^2 + (Im)^2$. To create an artificial Fourier transform, $(Re)^2$ was randomized from zero to $Power$, while $(Im)^2 = Power - (Re)^2$. The square roots of $(Re)^2$ and $(Im)^2$ were assigned a random sign (negative or positive) and form the real and imaginary parts of the first half of the artificial Fourier transform. The second half of the artificial Fourier transform was formed by flipping the complex conjugate of the first half, which preserves the symmetrical nature of Fourier transforms. The inverse

transform of the artificial Fourier transform gives back randomized OLR anomalies with the same power spectrum as the original Kelvin wave Fourier-filtered OLR anomalies. The artificial Fourier transforms do not preserve any real spatial coherence or longitudinal correlations, since they are intended to simulate random signals with the same power spectrum so that any correlations observed must emerge from random chance. Time-lagged variable regressions between winds and geopotential and the randomized OLR anomalies from the artificial Fourier transforms were repeated 1000 times. This creates a null distribution we can use to compare with the actual reconstructed wave winds and geopotential. If the original three points used to calculate the phase speeds fall outside the 95th percentile range of the null distribution, then the phase speeds are considered statistically significant, and the null hypothesis is rejected.

3. Results

3.1. Horizontal Structure of Zonal Winds and Geopotential Associated with Kelvin Waves

To begin, we investigate sample Hovmöller diagrams and horizontal regression maps of the reconstructed wave disturbances to determine the extent to which the associated zonal winds and geopotential match a classical Kelvin wave. Figure 3 shows the Hovmöller diagrams of 200 hPa zonal winds and geopotential associated with a reconstructed disturbance over the East Pacific Ocean during different background wind shear conditions. During wind shear 10 m/s, we observed in-phase (same sign) zonal winds and geopotential propagating eastward together, indicative of previously observed Kelvin waves [1]. However, during wind shear 20 m/s, we observed out-of-phase (opposite sign) signals mixed in with the in-phase zonal winds and geopotential, indicative of an eastward-advected Rossby wave mixed with a Kelvin wave due to stronger upper-level westerlies.



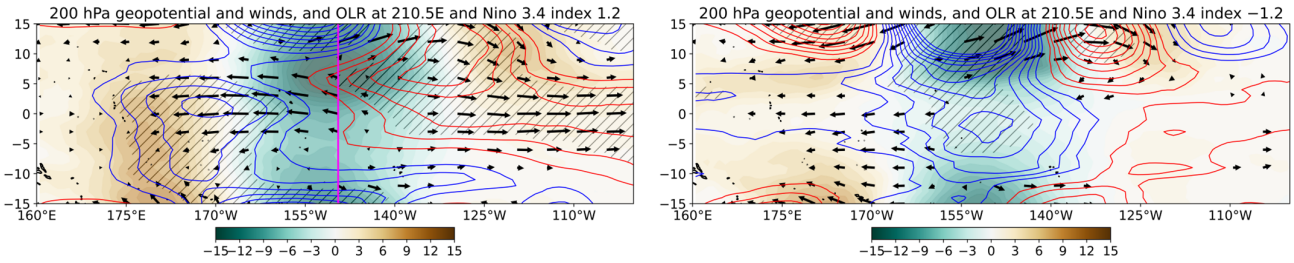
(**a**) Kelvin wave during wind shear 10 m/s

(**b**) Kelvin wave during wind shear 20 m/s

Figure 3. Hovmöller diagrams of zonal winds (m/s shading) and geopotential (3 m^2s^{-2} contours) associated with a 200 hPa wave disturbance passing through base longitude 230.5° E (dashed vertical line) during background vertical wind shear at (**a**) 10 m/s and (**b**) 20 m/s. Blue and red contours denote negative and positive geopotential anomalies, respectively. Hatches and pink dots indicate statistically significant zonal wind and geopotential, respectively, at 95% confidence. Phase speeds were calculated following the best-fit line at time lag −1, 0, 1 (black dots).

Strong La Niña events can also trigger eastward-advected Rossby waves. Figure 4 shows the horizontal maps of OLR, as well as 200 hPa winds and geopotential of the same reconstructed disturbance during strong ENSO. During strong El Niño conditions, we observe clear Kelvin wave features: in-phase zonal winds and geopotential, extratropi-

cal gyres, and a slightly northward-shifted convection (negative OLR) attributed to the ITCZ [2]. However, during strong La Niña conditions, we observe an extratropical Rossby wave train breaking equatorward and impeding on the Kelvin wave, thereby losing its statistical stability [36,37]. Evidently, certain background environments can lead to unfavorable conditions for the formation of a clear, strong Kelvin wave signal. Thus, the succeeding phase speed climatologies also indicate how well the zonal winds and geopotential reconstructed by the variable regression model match a classical Kelvin wave [22], and the statistical stability of the calculated phase speeds. Sections 3.2–3.4 are organized to cover the effects of overall background wind shear, intraseasonal wind shear, and interannual wind shear on the behavior of Kelvin waves over the West and East Pacific basins.



(**a**) Kelvin wave during strong El Niño

(**b**) Kelvin wave during strong La Niña

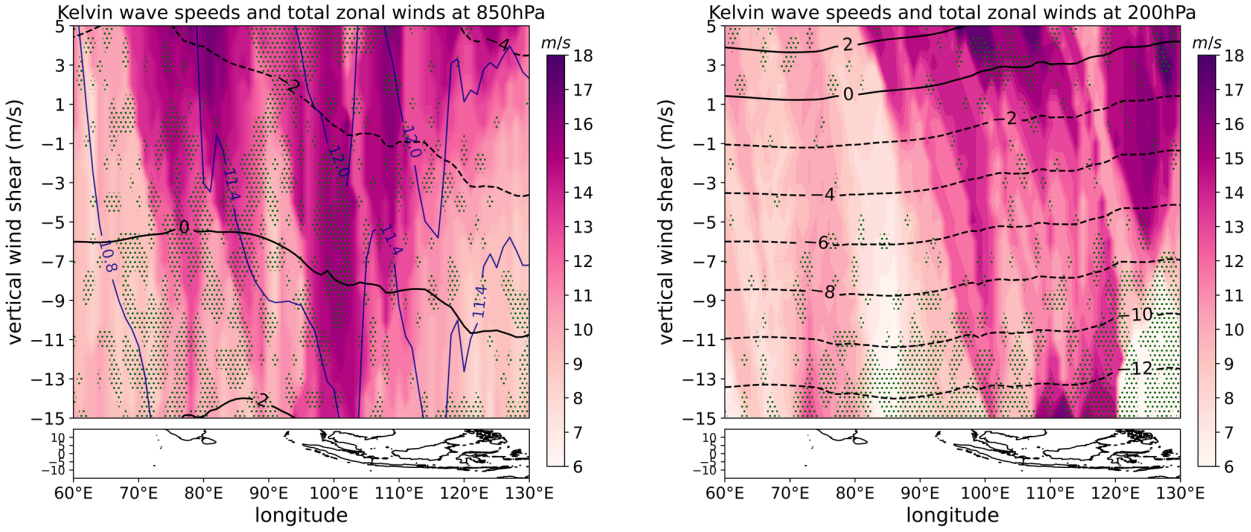
Figure 4. Horizontal maps of associated OLR (W/m^2 shading) and geopotential (5 m^{2}s^{-2} contours) for a 200 hPa wave disturbance passing through 210.5° E (pink vertical line) during strong (**a**) El Niño and (**b**) La Niña conditions. Blue and red contours denote negative and positive geopotential anomalies, respectively. Only the statistically significant winds are plotted in vectors, and gray hatching indicates statistically significant geopotential at 95% confidence.

3.2. Kelvin Wave Phase Speeds During Different Background Wind Shear Conditions

Figure 5 shows the phase speed climatology of the disturbances reconstructed by the variable regression model during a range of vertical wind shears over the West Pacific basin. Looking at regions without dots, the model reconstructs 850 hPa signals consistent with Kelvin waves outside of the Central Indian Ocean (70–80° E) and 200 hPa signals consistent with Kelvin waves during vertical wind shear above −11 m/s or upper-level zonal winds above −10 m/s. Horizontal regression maps around the Central Indian Ocean during strong easterly shear (Figure A1) show that the 850 hPa westerlies associated with the Kelvin wave tend to shift eastward and coincide with the center of convection, like previous observations [24]. Thus, the 850 hPa Kelvin wave ridge and trough tend to both coincide with westerlies near the base longitude, leading to a weaker positive correlation between zonal winds and geopotential.

Looking at the contours in Figure 5a, the fastest 850 hPa Kelvin waves tend to coincide with weak easterlies and more moist conditions, which contradicts the hypotheses that a headwind and increased static stability felt by Kelvin waves slow them down [18,38]. However, Ref. [39] showed that increased low-level moisture in the Indian Ocean tends to coincide with weaker than average upper-level easterlies, which increases the wave's eastward propagation speed. This suggests strong coupling between the upper- and lower-tropospheric components of the Kelvin wave, since its lower-tropospheric components tend to respond to upper-level background wind forcing. Furthermore, over the East Indian Ocean (70–90° E), upper-tropospheric Kelvin waves tend to propagate more slowly than lower-tropospheric Kelvin waves during the same shear, because of stronger upper-level easterlies stalling the former. To look more closely at the vertical structure, we plotted in Figure 6 the Kelvin wave zonal winds and geopotential during different vertical wind shear conditions over the East Indian Ocean. Following the shading along the pink line, the center of 850 hPa wind convergence remains the same, while the 200 hPa wind divergence

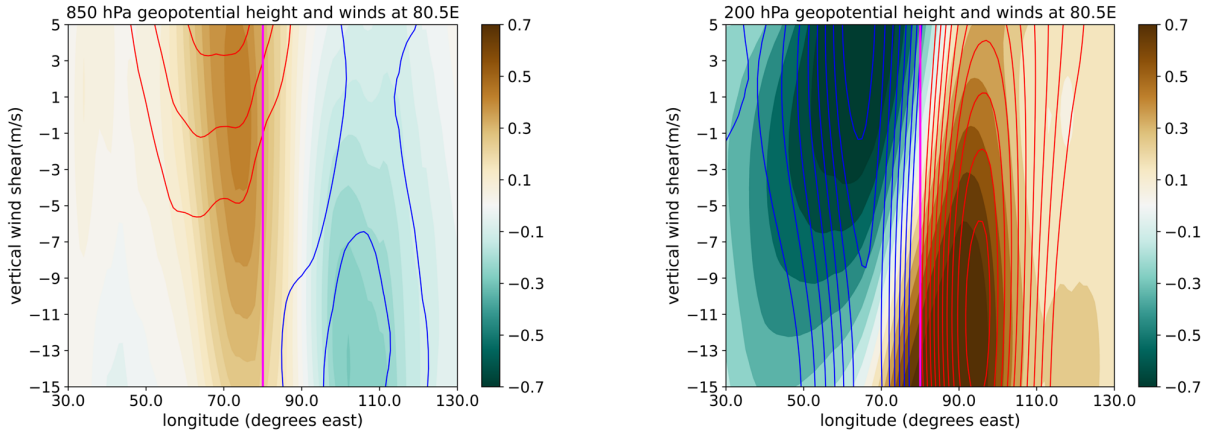
shifts more westward, so we get Kelvin waves with a stronger westward vertical tilt during more easterly shear. Interestingly, the locations of the ridge and trough (contours) remain the same, indicating zonal winds and geopotential becoming more out-of-phase at 200 hPa during stronger easterly shear.



(**a**) Phase speeds at 850 hPa

(**b**) Phase speeds at 200 hPa

Figure 5. (**a**) Lower and (**b**) upper tropospheric regressed wave phase speeds during different vertical wind shear over the West Pacific basin. The associated total specific humidity (in blue) and zonal wind (in black) are plotted in contours every 0.5×10^{-3} kg/kg and every 2 m/s, respectively. Solid lines indicate positive values, while dashed lines indicate negative values. Regions without dots indicate statistically significant phase speed calculations with 95% confidence and strong positive correlation above the 10th percentile between zonal winds and geopotential.



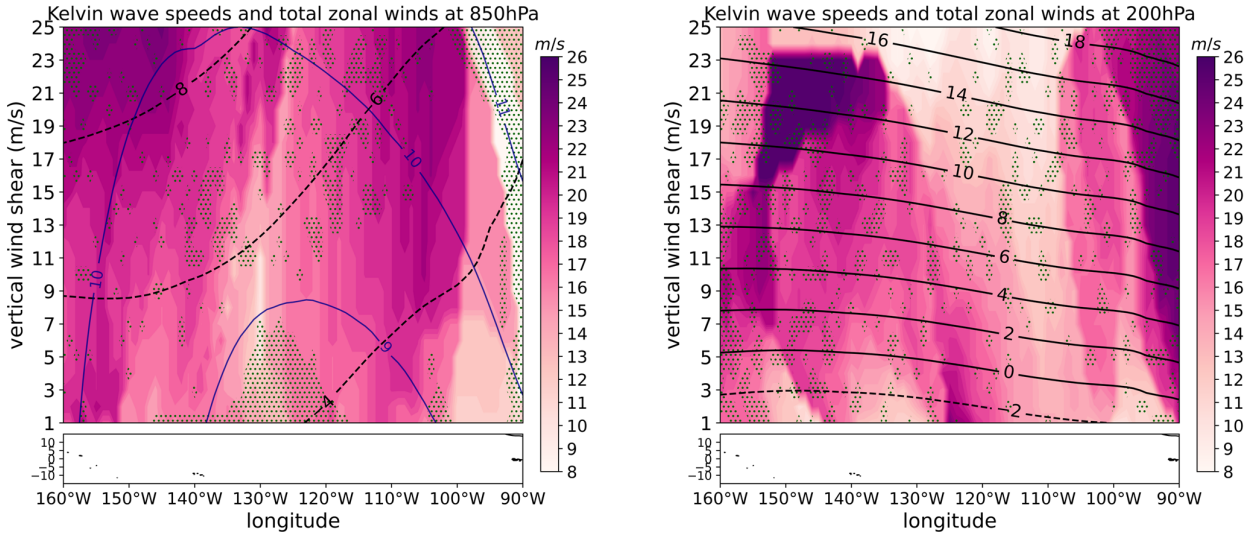
(**a**) 850 hPa Kelvin wave

(**b**) 200 hPa Kelvin wave

Figure 6. (**a**) Lower and (**b**) upper tropospheric wave disturbance geopotential (5 $m^2 s^{-2}$ contours) and zonal winds (shading, m/s) during different vertical wind shear at base longitude 80.5° E (pink vertical line). These were averaged at 15° S to 15° N during time lag zero. Red contours indicate positive values, while blue contours indicate negative values.

Figure 7 shows the phase speed climatology of the disturbance reconstructed by the variable regression model during a range of vertical wind shears over the East Pacific basin. Looking at regions without dots, the model generally reconstructs clear and strong 850 and 200 hPa Kelvin wave signals over the East Pacific. However, during the strongest westerly shear (>20 m/s), more extratropical Rossby waves transition equatorward and

trigger tropical cloud plumes [23]. The eastward-advected Rossby waves mix in with the Kelvin waves (see Figure 3), effectively slowing down the net signal and losing its classical structure.



(**a**) Phase speeds at 850 hPa

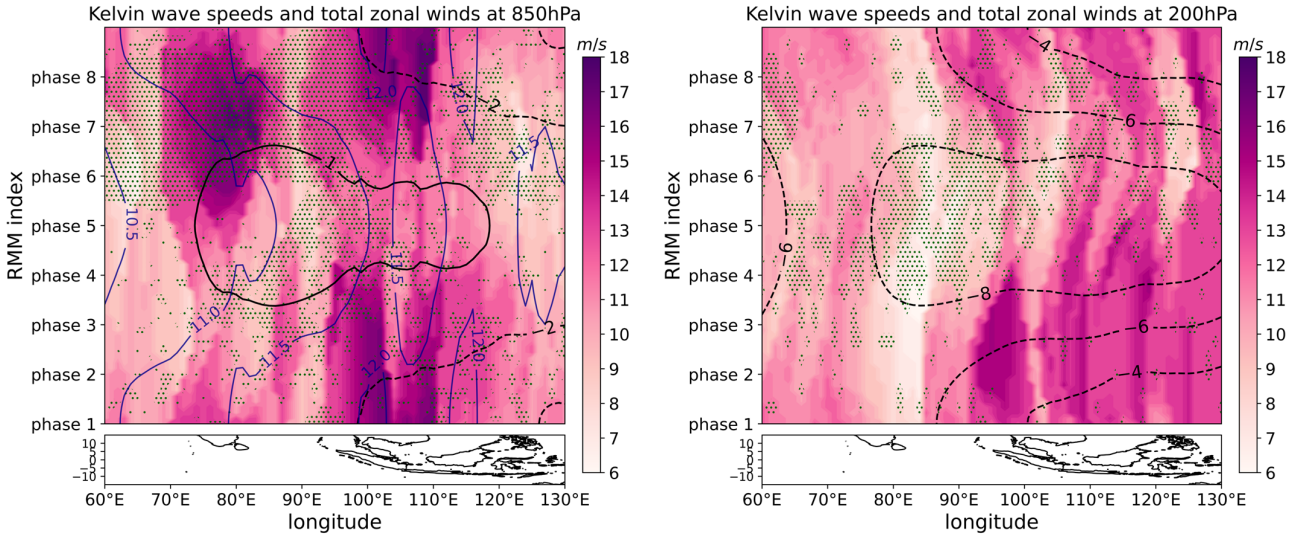
(**b**) Phase speeds at 200 hPa

Figure 7. Same as Figure 5, but over the East Pacific basin.

Like the West Pacific basin, we observe faster 850 hPa Kelvin waves during stronger easterlies and more moist conditions. This becomes less apparent closer to the west coast of South America (90° W), because the wave's leading winds (850 hPa easterlies) start interacting with the complex topography of the Andes. Kelvin wave 850 hPa winds can be blocked or diverted around mountains, lagging behind their 200 hPa components [12,40]. Furthermore, low-level background winds become more zonal (less meridional variability) towards the Central Pacific but acquire an equatorward component closer to South America [41,42]. On the other hand, we observe faster 200 hPa Kelvin waves during stronger westerly vertical shear, since the wave experiences a stronger upper tropospheric tailwind. We have looked at the overall effects of changes in background wind shear on Kelvin wave behavior. We now investigate the effects of the MJO, a major tropical intraseasonal oscillation that can modify background wind shear and moisture, on Kelvin wave behavior.

3.3. Kelvin Wave Phase Speeds During Different Convective Phases of the MJO

Figure 8 shows the phase speed climatology of the disturbance reconstructed by the variable regression model during different RMM phases over the West Pacific basin. Looking at regions without dots, the model generally reconstructs clear 850 hPa Kelvin wave signals during the MJO's enhanced phases (phases 3–5), and clear 200 hPa Kelvin wave signals during the MJO's suppressed phases (phases 1–2, 7–8). Hovmöller diagrams around the East Indian Ocean (Figure A2) show weaker 850 hPa easterlies shifted eastward towards the Maritime Continent's complex topography during the MJO's suppressed phases, leading to weaker statistical stability. Weaker eastward-shifted 850 hPa zonal winds match previous observations of Kelvin waves during the MJO's suppressed phases [24,43]. The most unclear 200 hPa Kelvin wave signals occur when coinciding with the MJO's enhanced phases (phases 3–5) over the East Indian Ocean and Maritime Continent (80–120° E), where the wave experiences the strongest background easterlies (<−8 m/s), which matches results from Figure 5a.



(**a**) Phase speeds at 850 hPa

(**b**) Phase speeds at 200 hPa

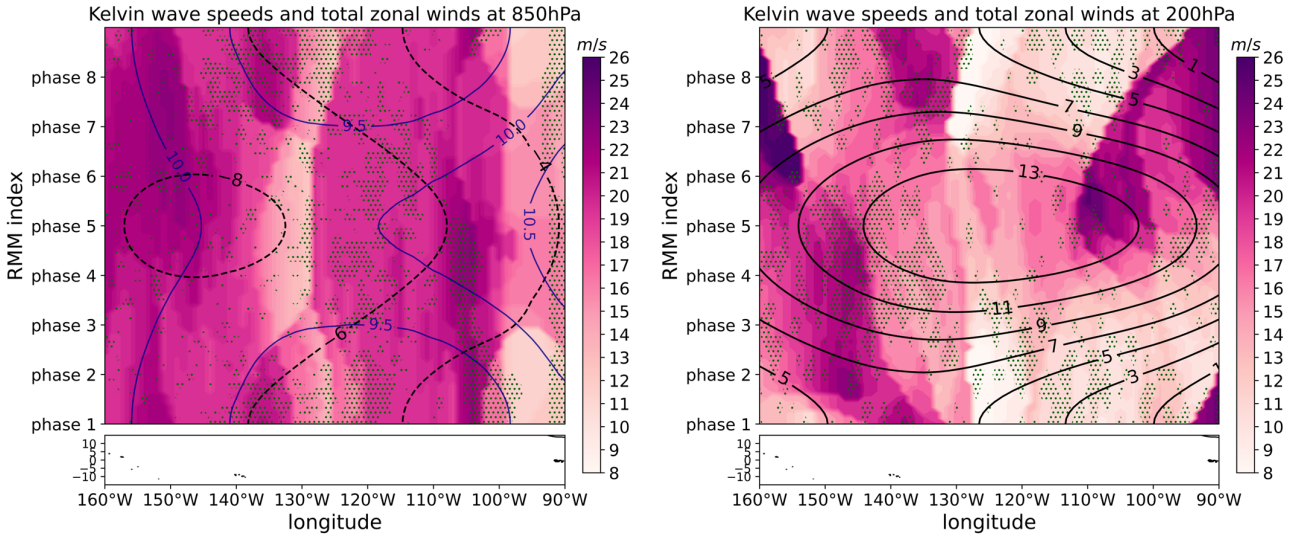
Figure 8. (**a**) Lower- and (**b**) upper-tropospheric regressed wave phase speeds during different RMM phases over the West Pacific basin. The associated total specific humidity (in blue) and zonal wind (in black) are plotted in contours every 0.5×10^{-3} kg/kg and every 2 m/s, respectively. Solid lines indicate positive values, while dashed lines indicate negative values. Regions without dots indicate statistically significant phase speed calculations with 95% confidence and strong positive correlation above the 10th percentile between zonal winds and geopotential.

Based on the contours of total zonal wind, 850 hPa westerlies and 200 hPa easterlies accompany the MJO's enhanced convective phases (phases 3–6), and vice versa, matching previous studies [16]. Lower-tropospheric Kelvin waves generally speed up when coinciding with easterlies and more moist conditions, just like in Figure 5a. On the other hand, 200 hPa Kelvin waves tend to slow down when coinciding with stronger background easterlies (headwind) during the MJO's enhanced phases (phases 3–5). Stronger zonal wind variability in different MJO phases generates more 200 hPa Kelvin wave phase speed variability over the Maritime Continent (90–130° E) than the East Indian Ocean (60–90° E). Furthermore, the complex topography of the Maritime Continent and the diverging winds from the rising branch of the Walker Circulation likely cause the sharp gradient of phase speeds around 90° E [44].

Figure 9 shows the phase speed climatology of the disturbance reconstructed by the variable regression model during different RMM phases over the East Pacific basin. Looking at regions without dots, the model generally reconstructs clear 850 hPa and 200 hPa Kelvin wave signals over the East Pacific basin. However, around 90° W, the wave's leading 850 hPa easterlies are blocked by the Andes a day after passing the base longitude, leading to weaker statistical stability. Furthermore, at 200 hPa around 150–140° W, extratropical Rossby wave trains intrude onto the equator, leading to weaker Kelvin signals. Likely, the strong upper-level westerlies during the MJO's suppressed phases (phases 2–5) can advect Rossby waves eastward over the Central Pacific, much like the results for strong La Niña conditions in Figure 4b.

Over the East Pacific basin, low-level easterlies and upper-level westerlies also accompany the MJO's suppressed convective phases (phases 2–6) and vice versa, matching previous observations [45]. Like Figure 7a, 850 hPa Kelvin waves have less phase speed variability, ranging only from 20 to 24 m/s over the East Pacific, but the fastest waves tend to coincide with higher moisture and stronger easterlies during the MJO's suppressed phases (phases 2–6). Like the West Pacific basin, we observe fast 200 hPa Kelvin waves during the MJO's suppressed phases (phases 2–6), because of stronger westerlies or tail-

winds, and vice versa. We have looked at the overall and intraseasonal effects of changes in background wind shear on Kelvin wave behavior. We now investigate the effects of ENSO, a major tropical interannual oscillation that can modify background wind shear and moisture, on Kelvin wave behavior.



(**a**) Phase speeds at 850 hPa

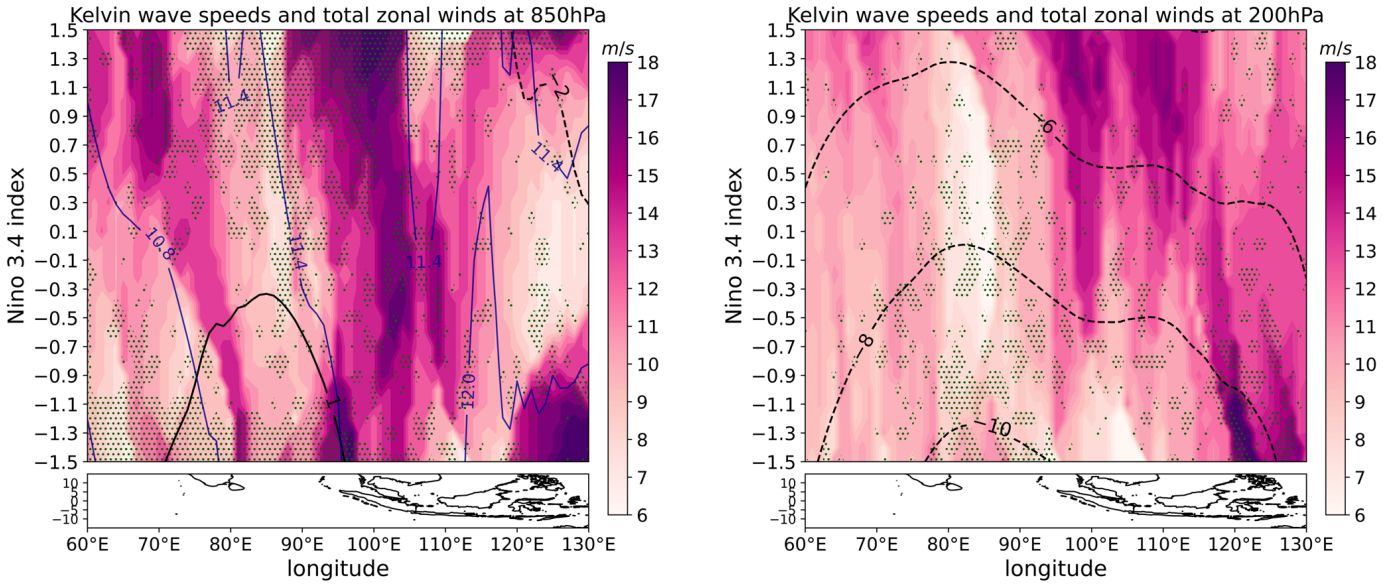
(**b**) Phase speeds at 200 hPa

Figure 9. Same as Figure 8, but over the East Pacific basin.

3.4. Kelvin Wave Phase Speeds During Different Convective Phases of ENSO

Figure 10 shows the phase speed climatology of the disturbance reconstructed by the variable regression model during different phases of ENSO over the West Pacific basin. A more positive and more negative Niño 3.4 index indicates stronger El Niño and La Niña conditions, respectively. Looking at regions without dots, the model generally reconstructs clear 850 hPa Kelvin wave signals during weak ENSO conditions and clear 200 hPa Kelvin wave signals during weak La Niña to strong El Niño conditions. The most unclear 850 and 200 hPa Kelvin wave signals occur during strong La Niña conditions over the East Indian Ocean (80–90° E), where there are strong upper-level easterlies (<−10 m/s), similar to results from Figures 5a and 8a. Furthermore, the 200 hPa diverging winds associated with the Kelvin wave tend to shift west of the base longitude during strong La Niña conditions, leading to a more westward vertical tilt like in Figure 6. This leads to weaker positive correlations between the slightly out-of-phase geopotential and zonal winds around the base longitude at 200 hPa.

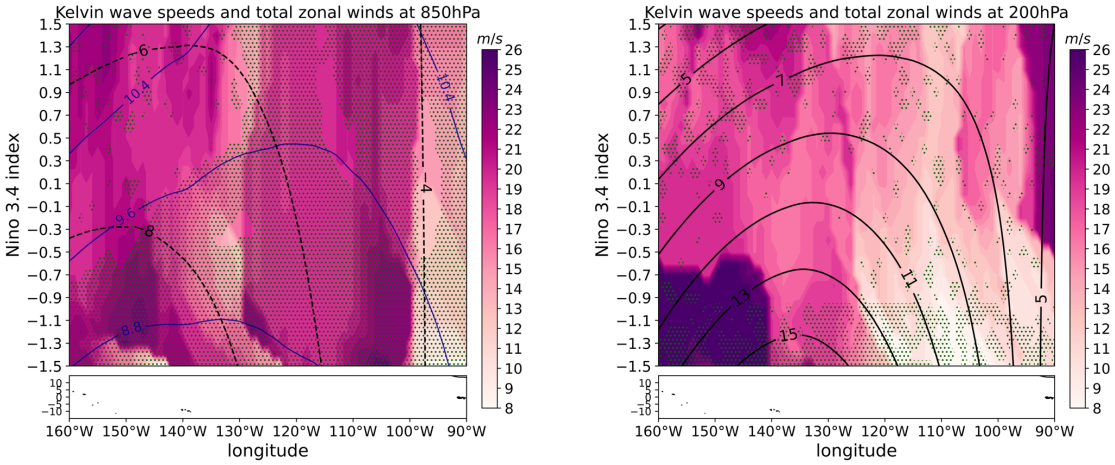
During El Niño conditions, we observe stronger westerly shear over the Indian Ocean but stronger easterly shear over the West Pacific Ocean, and vice versa occurs during La Niña conditions because of the overturning of the Walker Circulation [46]. Thus, we observe the fastest 200 hPa Kelvin waves during strong El Niño conditions (index > 1) over the Maritime Continent and during strong La Niña conditions (index < −1) over the West Pacific Ocean. Like Figures 5b and 8b, 200 hPa Kelvin waves over the East Indian Ocean and Maritime Continent have the most phase speed variability. On the other hand, variability in 850 hPa Kelvin waves depends more on their geographical location, as shown in the sharp change in phase speed at 90° E attributed to the Maritime Continent Barrier Effect [44]. The slowest statistically stable 850 hPa Kelvin waves tend to occur during weak ENSO conditions over the East Indian Ocean and the East Maritime Continent.



(**a**) Phase speeds at 850 hPa (**b**) Phase speeds at 200 hPa

Figure 10. (**a**) Lower- and (**b**) upper-tropospheric regressed wave phase speeds during different ENSO phases over the West Pacific basin. The associated total (**a**) specific humidity and (**b**) zonal wind are plotted in contours every 0.4×10^{-3} kg/kg and every 1 m/s, respectively. Regions without dots indicate statistically significant phase speed calculations with 95% confidence and strong positive correlations above the 10th percentile between zonal winds and geopotential.

Figure 11 shows the phase speed climatology of the disturbance reconstructed by the variable regression model during different phases of ENSO over the East Pacific basin. Looking at the dots, the model reconstructs weak 850 hPa Kelvin wave signals almost everywhere, except during strong El Niño conditions over the Central Pacific, likely because lower-level easterlies and cooler SSTs accompany La Niña—conditions unfavorable for strong Kelvin wave events. On the other hand, warmer SSTs, lower-level westerlies, and upper-level easterlies—conditions like the West Pacific basin—accompany strong El Niño conditions, allowing for the formation of stronger Kelvin waves [23,25]. Like Figure 9a, 850 hPa Kelvin waves have less phase speed variability, ranging only from 20 to 24 m/s, but the slowest waves tend to coincide with lower moisture and stronger easterlies during La Niña conditions over the Central Pacific Ocean. On the other hand, the model generally reconstructs clear 200 hPa Kelvin wave signals during El Niño conditions and weak La Niña conditions. During strong La Niña conditions, the stronger upper-level westerlies allow more extratropical Rossby waves to break equatorward towards the Central Pacific Ocean (see Figure 4), leading to signals less consistent with Kelvin waves and lower statistical stability.



(**a**) Phase speeds at 850 hPa (**b**) Phase speeds at 200 hPa

Figure 11. Same as Figure 10, but over the East Pacific basin.

4. Discussion and Conclusions

This work applied a time-lagged variable regression model to predict 850 hPa and 200 hPa Kelvin wave winds and geopotential, and to estimate their propagation speeds during different background vertical wind shear conditions, and MJO and ENSO phases between the West and East Pacific basins. Figure 12 summarizes the response of Kelvin waves to changes in the background conditions over the West and East Pacific basins. Overall, East Pacific Kelvin waves are faster than West Pacific Kelvin waves, because of climatological westerly shear in the former and easterly shear in the latter. Both upper- and lower-tropospheric Kelvin waves speed up when encountering 200 hPa westerlies (tailwind), and they slow down when encountering 200 hPa easterlies (headwind). The deceleration of Kelvin waves across the troposphere due to upper-level winds seems to overpower the acceleration by low-level zonal winds and moisture, and vice versa. This contradicts previous studies highlighting the effects of low-level moisture and static stability on the wave's phase speed [18,38]. However, in regions with strong convective coupling between the upper and lower troposphere, such as the East Indian Ocean, upper-tropospheric Kelvin waves tend to lock their phase speeds with and respond to dynamical forcing from lower-tropospheric Kelvin waves [5,16]. Under such conditions, background flow shifts the Kelvin wave's upper-level wind divergence westward or eastward, and changes its vertical tilt, but not so much its phase speed. Results suggest that the background flow likely has a greater effect on Kelvin wave circulation than moisture, since this work tracks the eastward propagation of Kelvin wave zonal winds. Other studies tracked the eastward propagation of convection and precipitation associated with convectively coupled Kelvin waves, and they found that increased convective heating and column moisture slow down Kelvin waves by decreasing the effective static stability [5,7,15,18]. Thus, future work could compare the effects of the background flow versus column moisture on the eastward propagation of Kelvin wave circulation versus convection, particularly in regions with strong coupling between the upper and lower troposphere.

This work also compared the effects of different RMM and ENSO phases on Kelvin wave phase speeds through changes in background wind shear and moisture. In general, Kelvin waves speed up during the MJO's suppressed convective phase, and slow down during the MJO's enhanced convective phase, due to changes in associated wind shear, which matches previous observations [24]. Furthermore, this work focuses more on synoptic Kelvin waves, which have been shown to be more sensitive to the effects of background wind shear than low-level moisture associated with the MJO [47]. Interestingly, Kelvin

waves and MJO propagation speeds respond similarly to moisture over the Indian Ocean. Ref. [39] found that the MJO speeds up during high moisture availability, because they coincide with weaker than usual upper-level easterlies, which matches our findings on Kelvin waves. Similar responses between Kelvin waves and the MJO motivate future work to investigate the effects of horizontal moisture advection and longwave radiation feedback on the propagation and maintenance of convectively coupled Kelvin waves as a moisture mode, much like the MJO [24,48]. This work focuses on Kelvin wave circulation instead of convection or precipitation, so gross moist static stability and moisture advection [7,48] likely are not observed as strong drivers of eastward propagation as the background flow. On the other hand, Kelvin wave phase speeds during different ENSO phases depend more on the associated vertical wind shear in different locations within the two basins. Overall, both upper- and lower-tropospheric Kelvin waves tend to speed up during MJO or ENSO phases that generate upper-tropospheric westerlies, and they slow down during upper-tropospheric easterlies. Thus, the enhanced convective phases of the MJO and El Niño are more likely to allow slow Kelvin waves to bring stronger winds and rainfall over the Pacific basin. Conversely, the locally suppressed convective phases of the MJO and La Niña are more likely to allow fast Kelvin waves to bring weaker winds and rainfall over the Pacific basins.

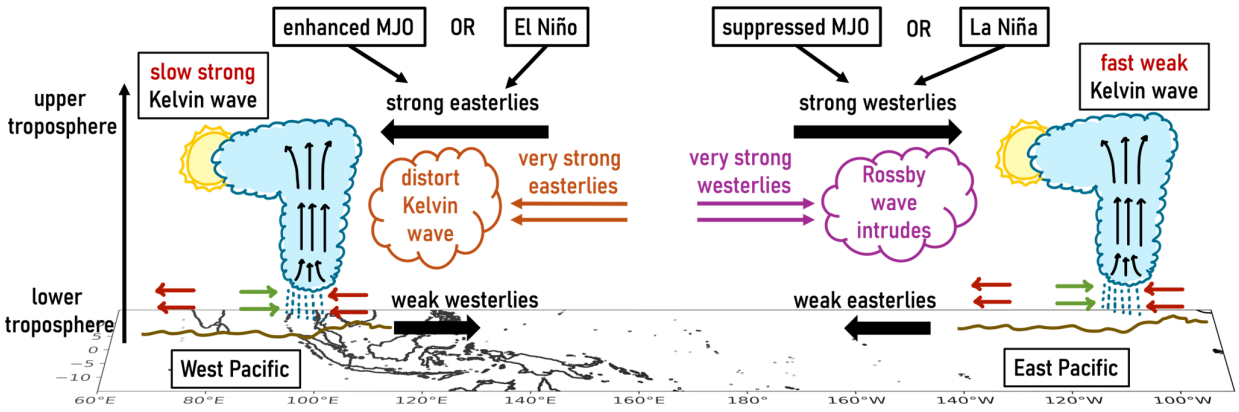


Figure 12. Conceptual diagram summarizing the response of atmospheric Kelvin waves to changes in background conditions over the West and East Pacific basins.

The strongest upper-level winds pose limits on the classical structure of Kelvin waves [22]. The strongest 200 hPa westerlies over the Central Pacific can allow extratropical Rossby waves to break equatorward and trigger tropical cloud plumes that can interfere with the Kelvin wave [23]. Upper-tropospheric Kelvin waves over the East Pacific may also evolve together with eastward-advected slow-moving Rossby waves during the strongest westerly shear [37]. On the other hand, during the strongest 200 hPa background easterlies over the West Pacific basin, the center of Kelvin wave wind divergence shifts westward, causing westerlies to cover the vicinity of the base longitude, leading to slightly out-of-phase zonal winds and geopotential. Ref. [6] also investigated the limits on retaining the classical structures of stratospheric Kelvin waves during extreme vertical shear conditions over the East Indian Ocean. They observed in-phase zonal winds and geopotential, indicative of a classical Kelvin wave, during strong background easterlies, but zonal winds and geopotential in quadrature during weak background easterlies. Interestingly, we observed the opposite in tropospheric Kelvin waves: zonal winds and geopotential in slight quadrature during strong background easterlies over the West Pacific basin. In general, classical Kelvin wave structures around the vicinity of the base longitude fall apart in 200 hPa easterlies stronger than −10 m/s over the West Pacific basin, and in 200 hPa westerlies stronger than 12 m/s over the East Pacific basin. Thus, the slowest Kelvin waves over

the West Pacific produce stronger winds and rainfall due to increased convective heating. On the other hand, the fastest Kelvin waves over the East Pacific produce weaker winds and rainfall but are compounded with the wind and rainfall caused by eastward-advected Rossby waves made possible by upper-tropospheric background westerly winds.

Overall, results suggest that weather prediction models need to resolve two components to accurately predict winds associated with Kelvin waves: (1) climatological vertical shear between the West and East Pacific basins and (2) the strong dependence of Kelvin waves on upper-level background flow. To further explore the disparity between the effects of background flow at different heights on Kelvin wave phase speed variability, future work will assess the contributions of advection by the background flow at different heights and moist processes at lower levels. Future work will also investigate the vertical propagation of Kelvin wave signals between the lower and upper troposphere in different background conditions, and the response of Kelvin wave phase speeds to meridional shear of background zonal flow.

Author Contributions: Conceptualization, C.M.D.C. and P.E.R.; Methodology, C.M.D.C. and P.E.R.; Validation, C.M.D.C. Formal analysis, C.M.D.C.; Investigation, C.M.D.C.; Writing—original draft, C.M.D.C.; Writing—review & editing, C.M.D.C. and P.E.R.; Visualization, C.M.D.C.; Supervision, P.E.R.; Project administration, P.E.R.; Funding acquisition, P.E.R. All authors have read and agreed to the published version of the manuscript.

Funding: This material is based upon work funded by the United States National Science Foundation under Grants AGS2103624 and AGS2417971.

Data Availability Statement: ERA5 Reanalysis was accessed 19 February 2024 from the Copernicus Climate Change Service (https://cds.climate.copernicus.eu/), and OLR was accessed 14 June 2024 from NOAA's NCEI (https://www.ncei.noaa.gov/). We can provide the code upon request.

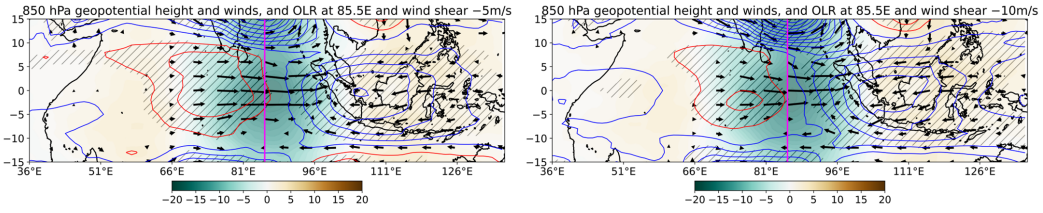
Conflicts of Interest: The authors declare no conflicts of interest.

Abbreviations

The following abbreviations are used in this manuscript:

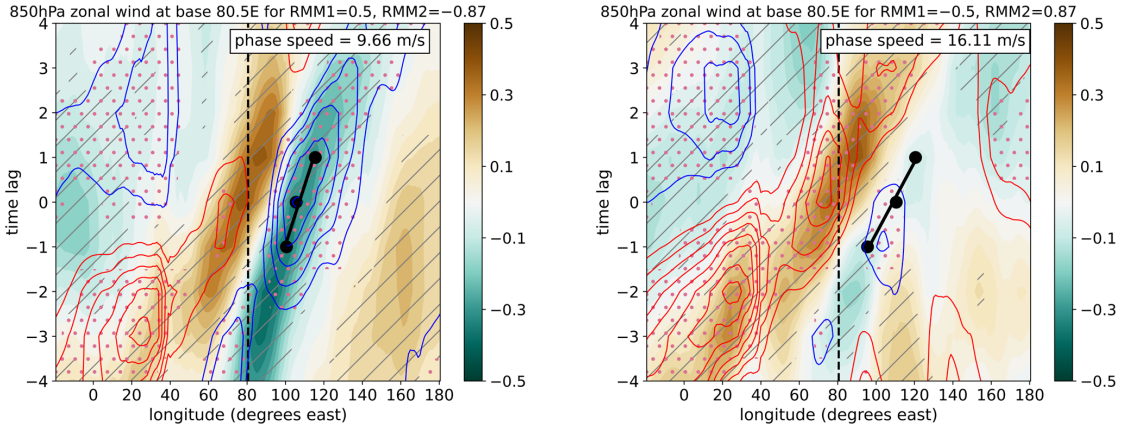
MJO	Madden–Julian Oscillation;
ENSO	El Niño–Southern Oscillation;
OLR	Outgoing Longwave Radiation;
RMM	Real-time Multivariate MJO;
SST	Sea Surface Temperature.

Appendix A. Horizontal Regression Maps and Hovmöller Diagrams



(**a**) Wind shear −5 m/s (**b**) Wind shear −10 m/s

Figure A1. Horizontal maps of associated OLR (W/m^2 shading) and geopotential (3 m^{2}s^{-2} contours) for an 850 hPa wave disturbance passing through 85.5° E (pink vertical line) during (**a**) −5 m/s and (**b**) −10 m/s. Blue and red contours denote negative and positive geopotential anomalies, respectively. Only the statistically significant winds are plotted in vectors, and gray hatching indicates statistically significant geopotential at 95% confidence.



(**a**) RMM phase 3 (**b**) RMM phase 7

Figure A2. Hovmöller diagrams of zonal winds (m/s shading) and geopotential (3 m^2s^{-2} contours) associated with an 850 hPa wave disturbance passing through base longitude 80.5° E (dashed vertical line) during the MJO's (**a**) enhanced and (**b**) suppressed convective phases. Blue and red contours denote negative and positive geopotential anomalies, respectively. Hatches and pink dots indicate statistically significant zonal wind and geopotential, respectively, at 95% confidence. Phase speeds were calculated following the best-fit line at time lag −1, 0, 1 (black dots).

References

1. Kiladis, G.N.; Wheeler, M.C.; Haertel, P.T.; Straub, K.H.; Roundy, P.E. Convectively coupled equatorial waves. *Rev. Geophys.* **2009**, *47*, 2003. [CrossRef]
2. Straub, K.H.; Kiladis, G.N. Observations of a Convectively Coupled Kelvin Wave in the Eastern Pacific ITCZ. *J. Atmos. Sci.* **2002**, *59*, 30–53. [CrossRef]
3. Lawton, Q.A.; Rios-Berrios, R.; Majumdar, S.J.; Emerton, R.; Magnusson, L. The representation of convectively coupled Kelvin waves in simulations with modified wave amplitudes. *J. Adv. Model. Earth Syst.* **2024**, *16*, e2023MS004187. [CrossRef]
4. Wheeler, M.; Kiladis, G.N.; Webster, P.J. Large-Scale Dynamical Fields Associated with Convectively Coupled Equatorial Waves. *J. Atmos. Sci.* **2008**, *57*, 613–640. [CrossRef]
5. Frierson, D.M.W.; Kim, D.; Kang, I.; Lee, M.; Lin, J. Structure of AGCM-Simulated Convectively Coupled Kelvin Waves and Sensitivity to Convective Parameterization. *J. Atmos. Sci.* **2011**, *68*, 26–45. [CrossRef]
6. Shaaban, A.A.; Roundy, P.E. On the interaction between Kelvin waves at different phase speeds and the background flow. *Q. J. R. Meteorol. Soc.* **2023**, *149*, 389–403. [CrossRef]
7. Frierson, D.M.W. Convectively Coupled Kelvin Waves in an Idealized Moist General Circulation Model. *J. Atmos. Sci.* **2007**, *64*, 2076–2090. [CrossRef]
8. Matthews, A.J. Dynamical propagation and growth mechanisms for convectively coupled equatorial Kelvin waves over the Indian Ocean. *Q. J. R. Meteorol. Soc.* **2021**, *147*, 4310–4336. [CrossRef]
9. Yang, G.; Hoskins, B.; Slingo, J. Convectively Coupled Equatorial Waves. Part II: Propagation Characteristics. *J. Atmos. Sci.* **2007**, *64*, 3424–3437. [CrossRef]
10. Straub, K.H.; Kiladis, G.N. The Observed Structure of Convectively Coupled Kelvin Waves: Comparison with Simple Models of Coupled Wave Instability. *J. Atmos. Sci.* **2003**, *60*, 1655–1668. [CrossRef]
11. Mekonnen, A.; Thorncroft, C.D.; Aiyyer, A.R.; Kiladis, G.N. Convectively Coupled Kelvin Waves over Tropical Africa during the Boreal Summer: Structure and Variability. *J. Clim.* **2008**, *21*, 6649–6667. [CrossRef]
12. Liebmann, B.; Kiladis, G.N.; Carvalho, L.M.; Jones, C.; Vera, C.S.; Bladé, I.; Allured, D. Origin of convectively coupled Kelvin waves over South America. *J. Clim.* **2009**, *22*, 300–315. [CrossRef]
13. Schreck, C.J. Kelvin Waves and Tropical Cyclogenesis: A Global Survey. *Mon. Wea. Rev.* **2015**, *143*, 3996–4011. [CrossRef]
14. Mayta, V.C.; Kiladis, G.N.; Dias, J.; Silva Dias, P.L.; Gehne, M. Convectively Coupled Kelvin Waves over Tropical South America. *J. Clim.* **2021**, *34*, 6531–6547. [CrossRef]
15. Wang, L.; Li, T. Roles of convective heating and boundary-layer moisture asymmetry in slowing down the convectively coupled Kelvin waves. *Clim. Dyn.* **2017**, *48*, 2453–2469. [CrossRef]
16. Aiyyer, A.; Molinari, J. MJO and Tropical Cyclogenesis in the Gulf of Mexico and Eastern Pacific: Case Study and Idealized Numerical Modeling. *J. Atmos. Sci.* **2008**, *65*, 2691–2704. [CrossRef]

17. Roose, S.; Ajayamohan, R.S.; Ray, P.; Mohan, P.R.; Mohanakumar, K. ENSO influence on Bay of Bengal cyclogenesis confined to low latitudes. *Clim. Atmos. Sci.* **2022**, *5*, 31. [CrossRef]
18. Kikuchi, K.; Kiladis, G.N.; Dias, J.; Nasuno, T. Convectively coupled equatorial waves within the MJO during CINDY/DYNAMO: Slow Kelvin waves as building blocks. *Clim. Dyn.* **2018**, *50*, 4211–4230. [CrossRef]
19. Rakhman, S.; Lubis, S.W.; Setiawan, S. Impact of ENSO on Seasonal Variations of Kelvin Waves and Mixed Rossby-Gravity Waves. *IOP Conf. Ser. Earth Environ. Sci.* **2017**, *54*, 012035. [CrossRef]
20. Wang, H.; Pan, Y.; Kumar, A.; Wang, W. Modulation of convectively coupled Kelvin wave activity in the tropical Pacific by ENSO. *Acta Meteorol. Sin.* **2013**, *27*, 295–307. [CrossRef]
21. Tulich, S.N.; Kiladis, G.N. On the regionality of moist Kelvin waves and the MJO: The critical role of the background zonal flow. *J. Adv. Model. Earth Syst.* **2021**, *13*, e2021MS002528. [CrossRef]
22. Matsuno, T. Quasi-Geostrophic Motions in the Equatorial Area. *J. Meteorol. Soc. Jpn.* **1966**, *44*, 25–43. [CrossRef] [PubMed]
23. Cheng, Y.; Tulich, S.; Kiladis, G.N.; Dias, J. Two Extratropical Pathways to Forcing Tropical Convective Disturbances. *J. Clim.* **2022**, *35*, 6587–6609. [CrossRef]
24. Neena, J.M.; Suhas, E.; Jiang, X. Modulation of the Convectively Coupled Kelvin Waves by the MJO over Different Domains. *J. Clim.* **2022**, *35*, 7025–7039.
25. Yang, G.; Hoskins, B. ENSO Impact on Kelvin Waves and Associated Tropical Convection. *J. Atmos. Sci.* **2013**, *70*, 3513–3532. [CrossRef]
26. Dias, J.; Gehne, M.; Kiladis, G.N.; Magnusson, L. The role of convectively coupled equatorial waves in Sub-Seasonal predictions. *Geophys. Res. Lett.* **2023**, *50*, e2023GL106198. [CrossRef]
27. Tulich, S.N.; Kiladis, G.N.; Suzuki-Parker, A. Convectively coupled Kelvin and easterly waves in a regional climate simulation of the tropics. *Clim. Dyn.* **2011**, *36*, 185–203. [CrossRef]
28. Lee, H.; NOAA CDR Program. NOAA Climate Data Record (CDR) of Daily Outgoing Longwave Radiation (OLR), Version 1.2. 2011. Available online: https://www.ncei.noaa.gov/access/metadata/landing-page/bin/iso?id=gov.noaa.ncdc:C00875 (accessed on 14 June 2024).
29. Copernicus Climate Change Service (C3S) Climate Data Store (CDS). ERA5 Hourly Data on Pressure Levels from 1940 to Present. 2023. Available online: https://cds.climate.copernicus.eu/datasets/reanalysis-era5-pressure-levels?tab=overview (accessed on 19 February 2024).
30. Wheeler, M.C.; Hendon, H.H. An all-season real-time multivariate MJO index: Development of an index for monitoring and prediction. *Mon. Wea. Rev.* **2004**, *132*, 1917–1932. [CrossRef]
31. Kaplan, A.; Cane, M.A.; Kushnir, Y.; Clement, A.C.; Blumenthal, M.B.; Rajagopalan, B. Analyses of global sea surface temperature 1856–1991. *J. Geophys. Res. Ocean.* **1998**, *103*, 18567–18589. [CrossRef]
32. Wheeler, M.; Kiladis, G.N. Convectively coupled equatorial waves: Analysis of clouds and temperature in the wavenumber–frequency domain. *J. Atmos. Sci.* **1999**, *56*, 374–399. [CrossRef]
33. Roundy, P.E. Diagnosis of seasonally varying regression slope coefficients and application to the MJO. *Q. J. R. Meteorol. Soc.* **2017**, *143*, 1946–1952. [CrossRef]
34. Weber, N.J.; Kim, D.; Mass, C.F. Convection–Kelvin Wave Coupling in a Global Convection-Permitting Model. *J. Atmos. Sci.* **2021**, *78*, 1039–1055. [CrossRef]
35. Roundy, P.E. Interpretation of the spectrum of eastward-moving tropical convective anomalies. *Q. J. R. Meteorol. Soc.* **2019**, *146*, 795–806. [CrossRef]
36. Kiladis, G.N. Observations of Rossby Waves Linked to Convection over the Eastern Tropical Pacific. *J. Atmos. Sci.* **1998**, *55*, 321–339. [CrossRef]
37. Matthews, A.J.; Kiladis, G.N. A Model of Rossby Waves Linked to Submonthly Convection over the Eastern Tropical Pacific. *J. Atmos. Sci.* **2000**, *57*, 3785–3798. [CrossRef]
38. Emanuel, K.A.; David Neelin, J.; Bretherton, C.S. On large-scale circulations in convecting atmospheres. *Q. J. R. Meteorol. Soc.* **1994**, *120*, 1111–1143. [CrossRef]
39. Shaaban, A.; Roundy, P.E. On the MJO Phase Speed among Different Background Moisture and Zonal Wind Base States. *J. Atmos. Sci.* **2025**, *82*, 301–317. [CrossRef]
40. Ridout, J.A.; Flatau, M.K. Convectively coupled Kelvin wave propagation past Sumatra: A June case and corresponding composite analysis. *J. Geophys. Res.* **2011**, *116*, D7. [CrossRef]
41. Kessler, W.S. The circulation of the eastern tropical Pacific: A review. *Prog. Oceanogr.* **2006**, *69*, 181–217. [CrossRef]
42. Amador, J.A.; Alfaro, E.J.; Lizano, O.G.; Magaña, V.O. Atmospheric forcing of the eastern tropical Pacific: A review. *Prog. Oceanogr.* **2006**, *69*, 101–142. [CrossRef]
43. Zhu, Y.; Li, T. Dynamic and thermodynamic modulations of the convectively coupled equatorial waves by the MJO. *Environ. Res. Commun.* **2021**, *3*, 025004. [CrossRef]

44. Abhik, S.; Hendon, H.H.; Zhang, C. The Indo-Pacific Maritime Continent Barrier Effect on MJO Prediction. *J. Clim.* **2023**, *36*, 945–957. [CrossRef]
45. Klotzbach, P.J.; Blake, E.S. North-Central Pacific Tropical Cyclones: Impacts of El Niño–Southern Oscillation and the Madden–Julian Oscillation. *J. Clim.* **2013**, *26*, 7720–7733. [CrossRef]
46. Lau, K.M.; Yang, S. Walker circulation. *Encycl. Atmos. Sci.* **2003**, *2505*, 00450-4.
47. Khouider, B.; Han, Y.; Majda, A.J.; Stechmann, S.N. Multiscale waves in an MJO background and convective momentum transport feedback. *J. Atmos. Sci.* **2012**, *69*, 915–933. [CrossRef]
48. Sobel, A.; Maloney, E. Moisture Modes and the Eastward Propagation of the MJO. *J. Atmos. Sci.* **2013**, *70*, 187–192. [CrossRef]

Disclaimer/Publisher's Note: The statements, opinions and data contained in all publications are solely those of the individual author(s) and contributor(s) and not of MDPI and/or the editor(s). MDPI and/or the editor(s) disclaim responsibility for any injury to people or property resulting from any ideas, methods, instructions or products referred to in the content.